



2 DOCTORAL THESIS

4 Optimisation studies and background
5 estimation in searches for the supersymmetric
6 partner of the top quark in all-hadronic final
7 states with the ATLAS Detector at the LHC

9 *A thesis submitted in fulfillment of the requirements
10 for the degree of Doctor of Philosophy*

11 *in the*

12 Experimental Particle Physics Research Group
13 School of Mathematical and Physical Sciences

14 *Author:*
15 Fabrizio MIANO

Supervisor:
Dr. Fabrizio SALVATORE

17th October 2017

Dedicated to my family.

*Have no fear for atomic energy
'cause none of them can stop the
time*

17

Robert Nesta Marley

18

Acknowledgments

¹⁹ Thanks to every single thing that went wrong. It made me stronger.

Declaration

21 I, Fabrizio MIANO, hereby declare that this thesis, titled, "Optimisation studies and back-
22 ground estimation in searches for the supersymmetric partner of the top quark in all-
23 hadronic final states with the ATLAS Detector at the LHC" has not been and will not be,
24 submitted in whole or in part to another University for the award of any other degree.

25 *Brighton, June 2018*

University of Sussex
School of Mathematical and Physical Sciences
Experimental Particle Physics Research Group

Doctoral Thesis

31
32 Optimisation studies and background estimation in searches for
33 the supersymmetric partner of the top quark in all-hadronic final
34 states with the ATLAS Detector at the LHC

36 by Fabrizio MIANO

Abstract

38 This thesis presents searches for supersymmetry in $\sqrt{s} = 13$ TeV proton-proton collisions
39 at the LHC using data collected by the ATLAS detector in 2015, 2016 and 2017. Events
40 with 4 or more jets and missing transverse energy were selected. Kinematic variables
41 were investigated and optimisations were performed to increase the sensitivity to su-
42 persymmetric signals. Standard Model backgrounds were estimated by means of Monte
43 Carlo simulations and data-driven techniques. Before analysing the data in the blinded
44 signal regions the agreement between data and background predictions and the extrapolations
45 from control and validation regions to signal regions were validated. The analysis
46 yielded no significant excess in any of the analyses performed. Therefore limits were
47 set and the results were interpreted as lower bounds on the masses of supersymmetric
48 particles in various scenarios and models.

49 **Contents**

50	Introduction	1
51	1 The Standard Model, Supersymmetry, and the motivations behind it	2
52	1.1 Overview	2
53	1.2 Limitations of the Standard Model	9
54	1.3 Supersymmetry	11
55	1.3.1 Why SUSY?	11
56	1.3.2 Minimal Supersymmetric Standard Model	11
57	1.3.3 R-parity SUSY	11
58	1.3.4 Simplified models	11
59	1.3.5 Phenomenological MSSM	11
60	2 The ATLAS Experiment at the LHC	12
61	2.1 The LHC	12
62	2.2 The ATLAS Detector	14
63	2.2.1 The Magnet System	16
64	2.2.2 The Inner Detector	17
65	2.2.3 The Calorimeters	20
66	2.2.4 The Muon Spectrometer	21
67	2.3 The ATLAS Trigger System	23
68	2.3.1 Level 1 Trigger	24
69	2.3.2 High-Level Trigger	24
70	3 The <i>b</i>-jet Trigger Signature in ATLAS	26
71	3.1 Trigger Efficiency	26
72	4 Event Simulation and Reconstruction	27
73	4.1 Event Generation	27

74	4.1.1 Parton Distribution Functions (PDFs)	27
75	4.1.2 Matrix Element Calculation	27
76	4.1.3 Parton Showers	27
77	4.1.4 Hadronisation	27
78	4.2 Detector Simulation	27
79	5 Stop searches in final states with jets and missing transverse energy	28
80	6 Results and Statistical Intepretations	29
81	Trigger	30
82	Bibliography	31

⁸³ List of Tables

⁸⁴	1.1 Forces and mediators described by the SM	5
---------------	--	---

List of Figures

<p>85 List of Figures</p> <p>86 1.1 The Higgs potential in the complex plane.</p> <p>87 1.2 Summary of several Standard Model total production cross section measurements, corrected for leptonic branching fractions, compared to the corresponding theoretical expectations. All theoretical expectations were calculated at NLO or higher. The luminosity used for each measurement is indicated close to the data point. Uncertainties for the theoretical predictions are quoted from the original ATLAS papers. They were not always evaluated using the same prescriptions for PDFs and scales. Not all measurements are statistically significant yet [1].</p> <p>94 9</p> <p>95 2.1 CERN Accelerator complex. The LHC is the last ring (dark grey line). Smaller machines are used for early-stage acceleration and also to provide beams for other experiments [2].</p> <p>96 14</p> <p>97 2.2 Cut-away view of the ATLAS detector. The dimensions of the detector are 25 m in height and 44 m in length. The overall weight of the detector is approximately 7000 tonnes [2].</p> <p>99 15</p> <p>101 2.3 The ATLAS magnet system.</p> <p>102 2.4 The ATLAS Inner Detector</p> <p>103 2.5 A computer generated image of the full calorimeter.</p> <p>104 2.6 Cut-away view of the ATLAS muon system [3].</p> <p>105 2.7 The ATLAS TDAQ system. L1Topo and FTK were being commissioned during 2015 and not used for the results shown in this thesis [4].</p> <p>106 23</p>	
--	--

¹⁰⁷ Introduction

¹⁰⁸ Last thing to write

¹⁰⁹ **Chapter 1**

¹¹⁰ **The Standard Model,
Supersymmetry, and the motivations
behind it**

¹¹³

A theory is something nobody believes, except the person who made it. An experiment is something everybody believes, except the person who made it.

Albert Einstein

¹¹⁴ The Standard Model (SM) of particle physics is an effective theory that aims to provide
¹¹⁵ a general description of fundamental particles and the phenomena we see in nature, i. e.
¹¹⁶ the way they interact. Unfortunately, our understanding of nature is still limited due to
¹¹⁷ some opened question to which the SM is not able to answer to, yet.

¹¹⁸ In this chapter, an overview of the SM will be presented in Section 1.1 together with
¹¹⁹ the limitations of such theory and some of the reasons behind the need of an extension.
¹²⁰ For the last decades theoretical physicsts have been trying to provide extensions to the
¹²¹ SM, the so-called beyond-the-SM theories. Among these, one of the most popular, Super-
¹²² symmetry which will be discussed in Section 1.3.

¹²³ **1.1 Overview**

¹²⁴ The 20th century can be considered a quantum revolution. Several experiments led to
¹²⁵ discoveries which were found to be, together with the formalised theory, a solid base of

¹²⁶ the Standard Model of particle physics and our description of nature. Several particles
¹²⁷ were predicted first by the SM and then experimentally observed e.g. the W and the Z
¹²⁸ bosons, the τ lepton, [5], and more recently the Higgs boson at the LHC discovered by
¹²⁹ ATLAS [6] and CMS [7].

¹³⁰ The SM lays on a Quantum Field Theory (QFT) where particles are treated like fields.
¹³¹ It can describe three of the four fundamental forces; weak, electromagnetic, and strong.
¹³² As of today, gravity is not considered in the SM. Sections 1.1 and 1.2 will be focused
¹³³ on the description of the fields together with the carriers of the information, and on the
¹³⁴ limitations that such theory implies, respectively.

¹³⁵ The most general classification of the particles within the SM can be made by means
¹³⁶ of spin. Fermions have half-integer spin values - and are usually referred to as matter -,
¹³⁷ and bosons have integer-spin values. A noteworthy subset of bosons is formed by the
¹³⁸ Spin-1 bosons (also known as gauge bosons). These can be considered the information
¹³⁹ carriers or, in fact, the mediators of the forces.

¹⁴⁰ Fermions

¹⁴¹ Six quarks and six leptons belong to the fermions family. In particular, fermions can be
¹⁴² grouped into three generations. Each generation contains four particles; one up- and
¹⁴³ one down-type quark, one charged lepton and one neutral lepton. The masses of the
¹⁴⁴ charged leptons and quarks increase with the generation. The six quarks of the SM can
¹⁴⁵ be grouped into three doublets:

$$\begin{pmatrix} u \\ d \end{pmatrix}, \quad \begin{pmatrix} c \\ s \end{pmatrix}, \quad \begin{pmatrix} t \\ b \end{pmatrix}$$

¹⁴⁶ The up-type quarks (up, charm, top) have charge $+\frac{2}{3}e$ and the down-type quarks (down,
¹⁴⁷ strange, beauty/bottom) have charge $-\frac{1}{3}e$, where e is the electron charge. Quarks also
¹⁴⁸ have another quantum number that can be seen as the analogue of the electric charge,
¹⁴⁹ which is the colour charge. This can exist in three different states; "red", "green" and
¹⁵⁰ "blue". Moreover, as a consequence of *confinement*, which will be discussed later on in
¹⁵¹ this section, quarks cannot exist as free particles. They rather group to form hadronic
¹⁵² matter, also known as *hadrons*. There are two kinds of hadrons; mesons and baryons.
¹⁵³ Mesons are quark-antiquark systems, e.g. the pion, and baryons are three-quark system,
¹⁵⁴ e.g. protons and neutrons. Quarks and anti-quarks have a baryon number of $\frac{1}{3}$ and $-\frac{1}{3}$,
¹⁵⁵ respectively.

¹⁵⁶ There are six leptons and they can be classified in charged leptons (electron e , muon
¹⁵⁷ μ , tau τ) and neutral leptons (electron neutrino ν_e , muon neutrino ν_μ , tau neutrino ν_τ).

$$\begin{pmatrix} \nu_e \\ e^- \end{pmatrix}, \quad \begin{pmatrix} \nu_\mu \\ \mu^- \end{pmatrix}, \quad \begin{pmatrix} \nu_\tau \\ \tau^- \end{pmatrix}$$

¹⁵⁸ Each lepton has a characteristic quantum number, called lepton number (L). Negatively
¹⁵⁹ (positively) charged leptons have $L = -1$ ($L = 1$) and neutral leptons have $L = 0$. The
¹⁶⁰ lepton number is conserved in all the interactions.

¹⁶¹ Forces of Nature

¹⁶² Forces in the SM are described by gauge theories, where the interactions is mediated by
¹⁶³ a vector gauge boson.

¹⁶⁴ The electromagnetic force is described by Quantum ElectroDynamics (QED) and, as
¹⁶⁵ its mediator is the photon (γ) which couples to charged particles, it only affects charged
¹⁶⁶ leptons and quarks, not neutrinos. They are instead affected by the weak force which is
¹⁶⁷ mediated by the bosons W^\pm and Z^0 .

¹⁶⁸ The weak interaction is associated with handedness (the projection of a particle spin
¹⁶⁹ onto its direction of motion). Both leptons and quarks have left- and right-handed com-
¹⁷⁰ ponents. However, only the left-handed (right-handed) component for neutrinos (anti-
¹⁷¹ neutrinos) has been observed. This means that nature prefers to produce left-handed
¹⁷² neutrinos and right-handed anti-neutrinos, which is the so-called parity violation.

¹⁷³ The strong interactions, mediated by the gluon (electrically neutral and massless), is
¹⁷⁴ described by Quantum ChromoDynamics (QCD). Its coupling increases with increasing
¹⁷⁵ distance and is smaller at short range. Moreover, due to gluon self interactions, two
¹⁷⁶ different phenomena arise; *confinement*: neither quarks nor gluons are observed as free
¹⁷⁷ particles, but only colourless “singlet” states can be observed as “jets”, namely collim-
¹⁷⁸ ated cone-shaped sprays of hadrons; *asymptotic freedom*: interactions between quarks and
¹⁷⁹ gluons become weaker as the energy scale increases and the corresponding length scale
¹⁸⁰ decreases.

¹⁸¹ Table 1.1 summarises the forces described in the SM and their mediators' main char-
¹⁸² acteristics. Finally, the gravitational force, which is believed to be mediated by the grav-
¹⁸³ iton, is not included in Table 1.1 as it is not part of the SM.

Table 1.1: Forces and mediators described by the SM

Force	Name	Symbol	Mass [GeV]	Charge
Electromagnetic	Photon	γ	0	0
Weak	W	W^\pm	80.398	$\pm e$
	Z	Z^0	91.188	0
Strong	Gluon	g	0	0

¹⁸⁴ Symmetries and Gauge Groups

¹⁸⁵ In 1915, the mathematician Emmy Noether (23 March 1882 – 14 April 1935) proved that
¹⁸⁶ every differentiable symmetry of the action - defined as the integral over space of a Lag-
¹⁸⁷ rangian density function - of a physical system has a corresponding conservation law.
¹⁸⁸ More generally, a symmetry is a property of a physical system. Under certain transfor-
¹⁸⁹ mations this property is preserved.

¹⁹⁰ A gauge theory in QFT, is a theory in which the Lagrangian is invariant under a
¹⁹¹ continuous group of local transformation. Group theory was then adopted to describe
¹⁹² the symmetries conserved in the SM. The gauge group of the theory is the *Lie Group*.
¹⁹³ It contains all the transformations between possible gauges. The Lie algebra of group
¹⁹⁴ generators is therefore associated with any Lie group and for each group generator there
¹⁹⁵ emerges a corresponding field: the gauge field. The quanta of the gauge fields are called
¹⁹⁶ *gauge bosons*.

¹⁹⁷ The three SM interactions can therefore be mathematically described by the following:

$$U(1)_Y \otimes SU(2)_L \otimes SU(3)_C \quad (1.1)$$

¹⁹⁸ Here, Y is the weak hypercharge, used to estimate the correlation between the electric
¹⁹⁹ charge (Q) and the third component of the weak isospin (I_3) via the relation $Q = I_3 + Y/2$,
²⁰⁰ where I_3 can either be $\pm 1/2$ or 0 for left-handed and right-handed particles, respectively;
²⁰¹ C the colour charge and L the left-handedness.

²⁰² As of today, we can describe three of the four forces of nature with group theory. QED
²⁰³ is an Abelian gauge theory with $U(1)$ as symmetry group, with the electromagnetic four-
²⁰⁴ potential as its gauge field and with the photon as its gauge boson [8]. The interactions
²⁰⁵ between charged fermions occurs by the exchange of a massless photon.

²⁰⁶ The weak interaction and the strong interactions are non-Abelian gauge theories with
²⁰⁷ gauge groups $SU(2)$ and $SU(3)$, respectively. As a consequence of being non-Abelian

208 the generators commutators are non-vanishing and therefore the gauge bosons can self-
 209 interact. The $SU(2)$ generators of the weak interaction are the massless gauge bosons
 210 $W_\mu^{\alpha=1,\dots,3}$ and, as mentioned earlier on in this chapter, they violate the parity by acting
 211 only on left-handed particles.

212 The gauge bosons of $SU(3)_C$ are eight massless gluons, $G_\mu^{\alpha=1,\dots,8}$. The strong interaction
 213 does not distinguish left- and right-handed particles. Finally, the Quarks that interact
 214 through weak interaction are mixtures of SM eigenstates as described by the CKM matrix
 215 [9].

216 Electroweak Symmetry Breaking and the Higgs mechanism

217 In 1979 Sheldon Glashow, Abdus Salam, and Steven Weinberg were awarded the Nobel
 218 Prize in Physics for their contributions to the so-called electroweak unification. In the
 219 mathematical description of the SM in 1.1 the electroweak interaction is described by
 220 $U(1)_Y \otimes SU(2)_L$. The electroweak physical bosons W , Z and γ are related to the four
 221 unphysical gauge bosons $W_\mu^{\alpha=1,\dots,3}$ and B_μ^0 . In particular, to obtain the physical bosons
 222 the gauge bosons have to mix as follows:

$$\begin{pmatrix} A_\mu \\ Z_\mu \end{pmatrix} = \begin{pmatrix} \cos \theta_W & \sin \theta_W \\ -\sin \theta_W & \cos \theta_W \end{pmatrix} \begin{pmatrix} B_\mu \\ W_\mu^3 \end{pmatrix} \quad (1.2)$$

223 Here, θ_W is the so-called *Weinberg angle* which is the angle by which spontaneous
 224 symmetry breaking rotates the original W_μ^3 and B_μ , producing the physical Z , and the
 225 photon. θ_W can be experimentally determined in terms of the coupling strengths of the
 226 $B_\mu(g_1)$ and the $W_\mu^\alpha(g_2)$ to the fermions using the relation $\tan \theta_W = g_1/g_2$. The field mixing
 227 of gauge bosons that gives birth to the physical ones can be mathematically expressed
 228 by the following:

$$A_\mu = W_\mu^3 \sin \theta_W + B_\mu \cos \theta_W \quad (1.3)$$

229

$$Z_\mu = W_\mu^3 \cos \theta_W - B_\mu \sin \theta_W \quad (1.4)$$

230 where A_μ and Z_μ represent the photon and the Z boson, respectively. The charged vector
 231 bosons, W_μ^\mp , and its complex conjugate are defined as:

$$W_\mu^\pm = \frac{1}{\sqrt{2}} (W_\mu^1 \mp i W_\mu^2) \quad (1.5)$$

²³² Mass terms for both gauge bosons and fermionic fields are not invariant under gauge
²³³ transformations and are therefore forbidden by the electroweak gauge. Nonetheless, it is
²³⁴ proven by experiments that W and Z are massive [8], therefore the SM assumption only
²³⁵ holds if the electroweak symmetry is broken.

²³⁶ The SM Lagrangian can be written as the sum of the various Lagrangians describing
²³⁷ the three interactions and the masses of the elementary particles as follows:

$$\mathcal{L}_{\text{SM}} = \mathcal{L}_{\text{EWK}} + \mathcal{L}_{\text{QCD}} + \mathcal{L}_{\text{Mass}} \quad (1.6)$$

²³⁸ In order for the SM Lagrangian to remain a renormalisable theory, mass terms ($\mathcal{L}_{\text{Mass}}$)
²³⁹ cannot be inserted by hand. A mechanism, that can preserve the gauge symmetry in
²⁴⁰ the SM and, that can solve the inconsistency arisen from the mass difference between
²⁴¹ the gauge bosons and the physical ones, is needed. A British theoretical physicist, Peter
²⁴² Higgs (29 May 1929, Newcastle upon Tyne, UK), came up with a brilliant solution for
²⁴³ which he was awarded the 2013 Physics Nobel Prize. In the 1960s, Higgs proposed that
²⁴⁴ broken symmetry in electroweak theory could explain the origin of masses of elementary
²⁴⁵ particles, and in particular of W and Z bosons: the Higgs mechanism was given birth.
²⁴⁶ The mechanism introduces a scalar field, known as the Higgs field, thought to couple to
²⁴⁷ both massive fermions and bosons.

²⁴⁸ In the SM the Higgs field is a doublet in $SU(2)$:

$$\phi = \begin{pmatrix} \phi^+ \\ \phi^0 \end{pmatrix} \quad (1.7)$$

²⁴⁹ with ϕ^+ and ϕ^0 being generic complex fields:

$$\phi^+ = \frac{\phi_1 + i\phi_2}{\sqrt{2}}, \quad \phi^0 = \frac{\phi_3 + i\phi_4}{\sqrt{2}} \quad (1.8)$$

²⁵⁰ Consider a Lagrangian of the form:

$$\mathcal{L}_{\text{Higgs}} = (\partial_\mu \phi)^* (\partial^\mu \phi) - V(\phi) \quad (1.9)$$

²⁵¹ Renormalizability and $SU(2)_L \otimes U(1)_Y$ invariance require the Higgs potential to be of
²⁵² the following form:

$$V(\phi) = \mu^2 \phi^\dagger \phi + \lambda (\phi^\dagger \phi)^2 \quad (1.10)$$

²⁵³ Eq. 1.9 is the Higgs Lagrangian if ϕ is chosen to be the following:

$$\phi = \begin{pmatrix} \phi^+ \\ \phi^0 \end{pmatrix} = \begin{pmatrix} G^+ \\ \frac{1}{\sqrt{2}}(v + H + iG^0) \end{pmatrix}$$

254 Here, the complex scalar field G^\pm and the real scalar field G^0 correspond to Goldstone
 255 bosons, and the real scalar field H is the SM Higgs boson field [10]. These massless scalars
 256 are absorbed due to the gauge transformations by the electroweak gauge bosons of the
 257 SM:

$$\phi = \begin{pmatrix} \phi^+ \\ \phi^0 \end{pmatrix} = \begin{pmatrix} 0 \\ \frac{1}{\sqrt{2}}(v + H) \end{pmatrix} \quad (1.11)$$

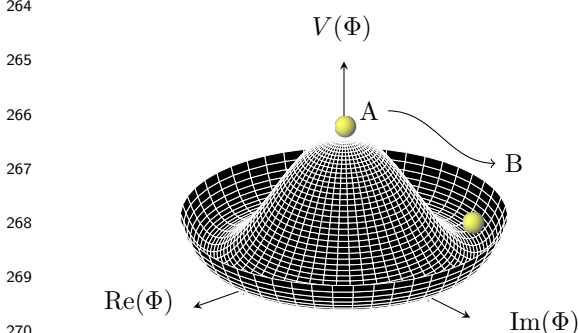
258 The Higgs potential in Eq. 1.10 is displayed in Fig. 1.1 if λ and μ are chosen to be real.
 259 Such potential has a non-zero ground state, v , also known as *vacuum expectation value*
 260 (VEV):

$$\phi_0 = \begin{pmatrix} 0 \\ \frac{1}{\sqrt{2}}v \end{pmatrix} \quad (1.12)$$

261 Such representation remains invariant under $U(1)$ allowing electric charge conservation.
 262 However, the SM gauge symmetry 1.1 is broken into $SU(2)_L \otimes U(1)_Y$.

263

In summary, to generate particle masses gauge symmetry must be broken. However, in order for the theory to remain renormalisable, the global Lagrangian symmetry must be preserved. This can be solved introducing the concept of *spontaneous symmetry breaking* (SSB): a mechanism that allows a symmetric Lagrangian, but not a symmetric VEV. In particular, given a Lagrangian invariant under a certain transformation, T_X and a generic set of states, that transform under T_X as the elements of a multiplet, the symmetry is spontaneously broken if one of those states is arbitrarily chosen as the ground state of the system. The interaction of the Higgs field with the $SU(2) \otimes U(1)$ gauge fields, $W_\mu^\alpha = 1, 2, 3$, result in the three gauge bosons fields acquiring mass whilst the B_0 field stays massless.



272 Figure 1.1: The Higgs potential in the complex plane.

273

274 eric set of states, that transform under T_X as the elements of a multiplet, the symmetry
 275 is spontaneously broken if one of those states is arbitrarily chosen as the ground state
 276 of the system. The interaction of the Higgs field with the $SU(2) \otimes U(1)$ gauge fields,
 277 $W_\mu^\alpha = 1, 2, 3$, result in the three gauge bosons fields acquiring mass whilst the B_0 field
 278 stays massless.

279 1.2 Limitations of the Standard Model

280 During Run 1 and 2 of the LHC, the SM has been extensively validated, as shown in
 281 Fig. 1.2: the agreement, between the measured production cross section of various SM
 282 processes and the SM predictions, looks very good. However, the reasons behind the
 283 mass difference between the three generations of fermions are still not explained by
 284 the SM because masses are treated as free parameters of the theory. In addition, there are
 285 some fundamental questions that have still no answer and they will be briefly discussed
 286 this section.

Standard Model Total Production Cross Section Measurements Status: July 2017

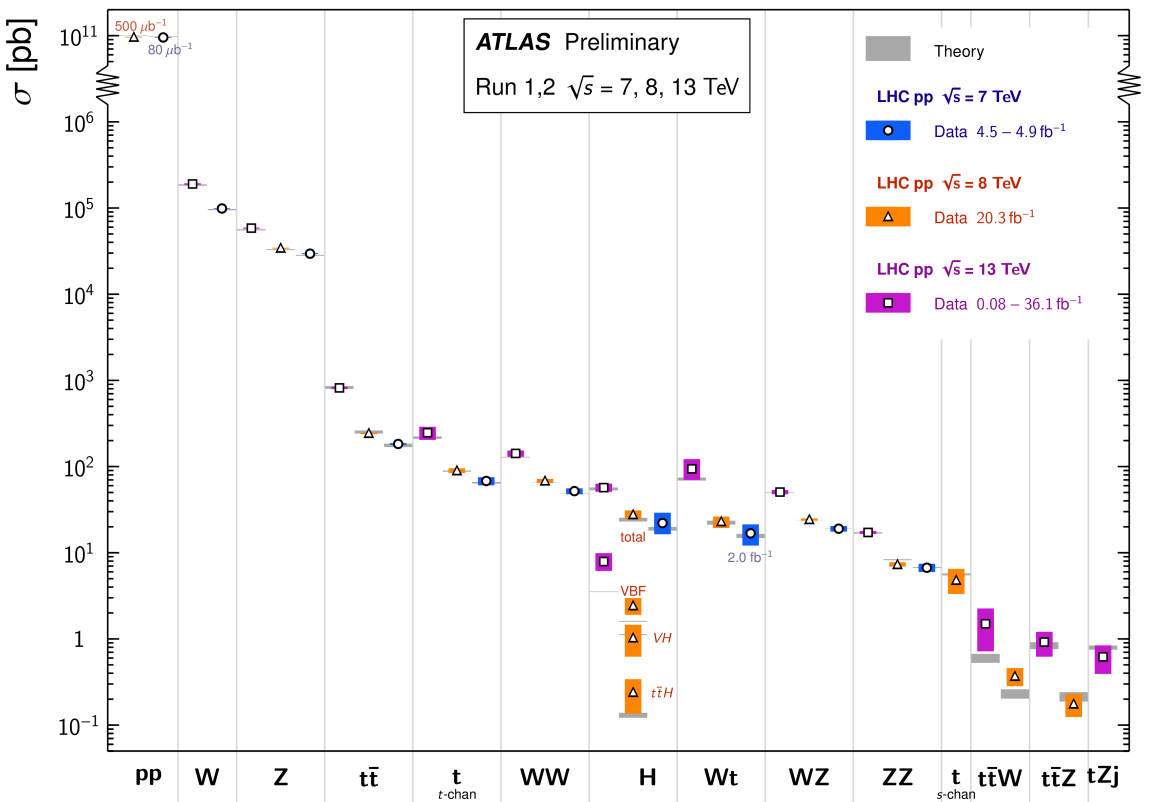


Figure 1.2: Summary of several Standard Model total production cross section measurements, corrected for leptonic branching fractions, compared to the corresponding theoretical expectations. All theoretical expectations were calculated at NLO or higher. The luminosity used for each measurement is indicated close to the data point. Uncertainties for the theoretical predictions are quoted from the original ATLAS papers. They were not always evaluated using the same prescriptions for PDFs and scales. Not all measurements are statistically significant yet [1].

²⁸⁷ **Hierarchy Problem**

²⁸⁸ The coupling of every particle to the Higgs field contributes to the mass of the Higgs
²⁸⁹ field, m_H^2 . In particular, The term due to fermionic loop coupling is given by:

$$\Delta m_H^2 = -\frac{|\lambda_f|^2}{8\pi^2} \Lambda_{\text{UV}}^2 + \dots, \quad (1.13)$$

²⁹⁰ where Λ_{UV} is the ultraviolet momentum cut-off, selected as the cut-off value for the loop
²⁹¹ integral. If Λ_{UV} laid somewhere around the Planck scale ($\sim 2 \cdot 10^{18}$ GeV), at which a QFT
²⁹² description of gravity is believed to become possible, then the correction to the Higgs
²⁹³ mass would be around 30 orders of magnitude larger than Higgs mass itself. However,
²⁹⁴ electroweak unification has been observed around $m_Z \sim O(100$ GeV) therefore, m_H^2 is not
²⁹⁵ a natural parameter. In other words, this difference between the electroweak scale and
²⁹⁶ the Planck scale arisen from the quantum corrections to the Higgs mass is the so-called
²⁹⁷ Hierarchy Problem [11].

²⁹⁸ **Neutrino Masses**

²⁹⁹ The Super-Kamiokande Collaboration first, in 1998 [12], and SNO Collaboration later, in
³⁰⁰ 2001 [13], have provided measurements of the neutrino flux from solar and atmospheric
³⁰¹ sources. The Nobel Prize in Physics 2015 was awarded jointly to Takaaki Kajita and Ar-
³⁰² thur B. McDonald “for the discovery of neutrino oscillations, which shows that neutrinos
³⁰³ have mass” [14]. Such feature contradicts the absence of a mechanism for mass genera-
³⁰⁴ tion for the neutrinos.

³⁰⁵ Various exotic solutions are on the market: one possible solution could be to add the
³⁰⁶ so-called Majorana mass terms for the neutrino (seesaw mechanism). Neutrino physics
³⁰⁷ could unveil physics beyond the SM.

³⁰⁸ **Dark Matter**

³⁰⁹ Although dark matter (DM) has never been directly observed, its existence is inferred
³¹⁰ from its gravitational effects. For example, looking at galaxies rotation, it was observed
³¹¹ that the rotation speed was higher than expected, given the amount of visible matter. Two
³¹² different reasoning arose during the last century to justify such effect either there is matter
³¹³ that cannot be seen by us (in terms of visible light), which contributes to the galacticis mass;
³¹⁴ or the general relativity works differently at galactic distances. The former is believed to

³¹⁵ be the most likely and it implies the existence of new particles which do not interact via
³¹⁶ electromagnetic interaction, the so-called Weakly Interacting Massive Particles (WIMPs).

³¹⁷ 1.3 Supersymmetry

³¹⁸ SUperSYmmetry (SUSY) is a theory that links gravity with the other fundamental forces
³¹⁹ of nature by introducing a space-time symmetry that relates bosons to fermions and vice-
³²⁰ versa, via a transformation of the form of:

$$Q |\text{fermion}\rangle = |\text{boson}\rangle, \quad Q |\text{boson}\rangle = |\text{fermion}\rangle \quad (1.14)$$

³²¹ For each SM particle there exists a superpartner (also referred to as *sparticle*) with a spin
³²² difference of $\Delta s = 1/2$. As of today, superpartners have not been observed yet, resulting
³²³ in the assumption that SUSY must be a broken symmetry, otherwise superpartners would
³²⁴ have had the same quantum numbers and masses as their SM equivalent. However,
³²⁵ if sparticles were to be too heavy the hierarchy problem would still remain unsolved.
³²⁶ The *soft* SUSY breaking mechanism overcomes this problem imposing contrains on the
³²⁷ masses of sparticles to a range that can be experimentally explored.

³²⁸ 1.3.1 Why SUSY?

³²⁹ bla

³³⁰ 1.3.2 Minimal Supersymmetric Standard Model

³³¹ bla

³³² 1.3.3 R-parity SUSY

³³³ bla

³³⁴ 1.3.4 Simplified models

³³⁵ bla

³³⁶ 1.3.5 Phenomenological MSSM

³³⁷ bla

³³⁸ **Chapter 2**

³³⁹ **The ATLAS Experiment at the LHC**

³⁴⁰ ATLAS (A Toroidal LHC ApparatuS) is one of the four main experiments (ATLAS, CMS,
³⁴¹ ALICE, LHCb) taking data at a center-of-mass energy of 13 TeV using beams delivered by
³⁴² the Large Hadron Collider (LHC). In this chapter an overview of the LHC will be given
³⁴³ in Section 2.1, then the ATLAS detector will be described in Section 2.2, and finally the
³⁴⁴ Trigger system, used to cleverly store the data, will be described in Section 2.3. A more
³⁴⁵ in-depth description of the Trigger algorithms I have been involved in will be given in
³⁴⁶ Chapter 3.

³⁴⁷ **2.1 The LHC**

³⁴⁸ As of today, the LHC is the world's largest and most powerful particle accelerator. It
³⁴⁹ was designed to help answer some of the fundamental open questions in particle phys-
³⁵⁰ ics by colliding protons at an unprecedented energy and luminosity. It is located at the
³⁵¹ European Organisation for Nuclear Research (CERN), in the Geneva area, at a depth ran-
³⁵² ging from 50 to 175 metres underground. It consists of a 27-kilometre ring made of su-
³⁵³ perconducting magnets, and inside it two high-energy particle beams travel in opposite
³⁵⁴ directions and in separate beam pipes.

³⁵⁵ The beams are guided around the ring by a strong magnetic field generated by coils -
³⁵⁶ made of special electric cables - that can operate in a superconducting regime. 1232 super-
³⁵⁷ conducting dipole and 392 quadrupole magnets, with an average magnetic field of 8.3 T,
³⁵⁸ are employed and kept at a temperature below 1.7 K, in order to preserve their supercon-
³⁵⁹ ducting properties. The formers are used to bend the beams and the latters to keep them
³⁶⁰ focused while they get accelerated.

³⁶¹ The collider first went live on September 2008 even though, due to a magnet quench

³⁶² incident that damaged over 50 superconducting magnets, it has been operational since
³⁶³ November 2009 when low-energy beams circulated in the tunnel for the first time since
³⁶⁴ the incident. This also marked the start of the main research programme and the begin-
³⁶⁵ ning of the so-called Run 1: first operational run (2009 - 2013).

³⁶⁶ Performance of the LHC

³⁶⁷ In June 2015 the LHC restarted delivering physics data, after a two-year break, the so-
³⁶⁸ called Long Shutdown 1 (LS1), during which the magnets were upgraded to handle the
³⁶⁹ current required to circulate 7-TeV beams. It was the beginning of the so-called Run 2 -
³⁷⁰ second operational run (2015-2018) - during which LHC has collided up to 10^{11} bunches
³⁷¹ of protons every 25 ns at the design luminosity - the highest luminosity the detector was
³⁷² designed to cope with - of $2 \cdot 10^{34} \text{ cm}^{-2} \text{s}^{-1}$. The definition of the luminosity is:

$$\mathcal{L} = f \frac{n_b N_1 N_2}{4\pi\sigma_x\sigma_y} \quad (2.1)$$

³⁷³ where N_1 and N_2 are the number of protons per bunch in each of the colliding beams, f
³⁷⁴ is the revolution frequency of the bunch collisions, n_b the number of proton per bunch,
³⁷⁵ and σ_x and σ_y are the horizontal and vertical dimensions of the beam. The luminosity is
³⁷⁶ strictly related to the number of collisions occurring during a certain experiment via the
³⁷⁷ following:

$$\mathcal{N}_{\text{event}} = \mathcal{L}\sigma_{\text{event}} \quad (2.2)$$

³⁷⁸ where σ_{event} is the cross section of the process under investigation. It has not only collided
³⁷⁹ protons but also heavy ions, in particular lead nuclei at $\sqrt{s_{NN}} = 5.02 \text{ TeV}$, at a luminosity
³⁸⁰ of $10^{27} \text{ cm}^{-2} \text{s}^{-1}$ [15].

³⁸¹ Acceleration stages

³⁸² Before reaching the maximum energy, the proton beams are accelerated by smaller ac-
³⁸³ celerators through various stages. Figure 2.1 shows a sketch of the CERN's accelerator
³⁸⁴ complex. It all begins at the linear accelerator LINAC 2. Here protons are accelerated up
³⁸⁵ to 50 MeV, and then injected in the Proton Synchrotron Booster (PSB) where they reach
³⁸⁶ 1.4 GeV. The next stage is the Proton Synchrotron (PS), which boosts the beams up to 25
³⁸⁷ GeV and then the Super Proton Synchrotron (SPS) makes them reach energies up to 450
³⁸⁸ GeV. Eventually, the beams are injected in bunches with a 25 ns spacing into the LHC,
³⁸⁹ where they travel in opposite directions, while they are accelerated to up to 13 TeV. Once

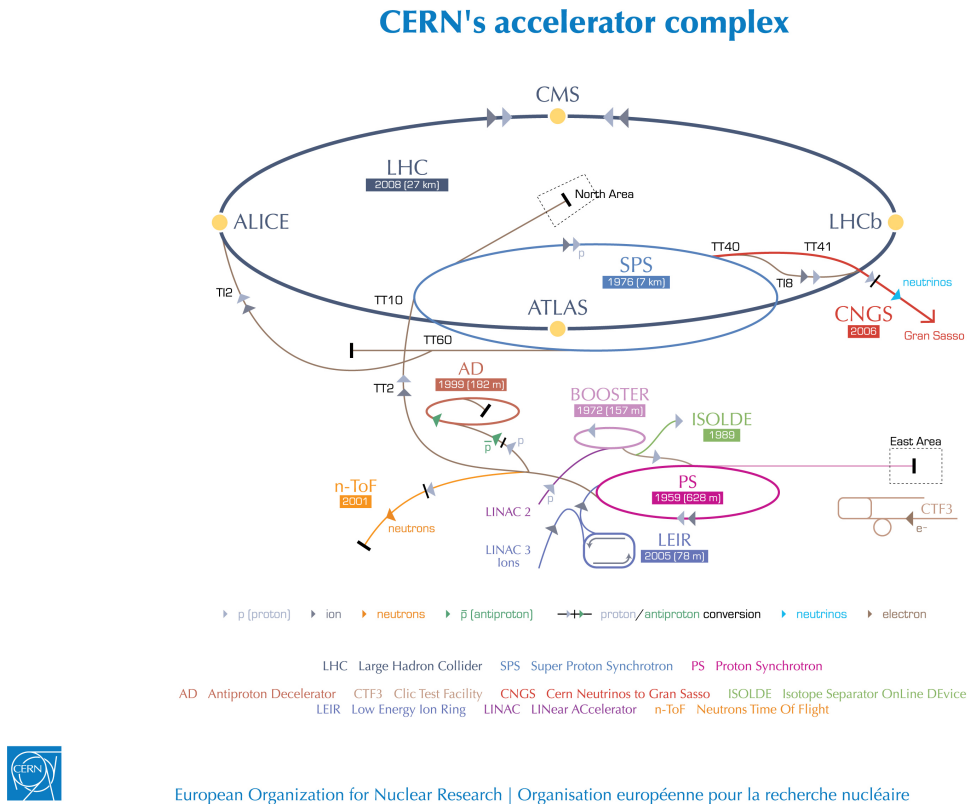


Figure 2.1: CERN Accelerator complex. The LHC is the last ring (dark grey line). Smaller machines are used for early-stage acceleration and also to provide beams for other experiments [2].

390 the bunches reach the maximum energy, they are made collide at four different points,
391 inside four experiments around the ring [16].

392 The heavy ion beams acceleration procedure is slightly different. Their journey starts
393 at LINAC 3 first, and the Low Energy Ion Ring (LEIR) then, before they make their way
394 into the PS where they follow the same path as the protons [16].

395 The four large detectors on the collision points are; the multi-purpose detectors A Tor-
396 oidal LHC ApparatuS (ATLAS), and Compact Muon Solenoid (CMS) [17], Large Hadron
397 Collider beauty (LHCb) [18], which focuses on flavour physics, and A Large Ion Collider
398 Experiment (ALICE) [19] which specialises in heavy ion physics. The *big four* are not the
399 only experiments at the CERN's accelerator complex. There also are smaller experiments
400 based at the the four caverns about the collision points e.g. TOTEM, LHCf and MoEDAL,
401 but this will not be discussed any further in this thesis.

402 2.2 The ATLAS Detector

403 ATLAS is a general-purpose detector designed to collect data with the highest luminosity
404 provided by the LHC. It is located at CERN's Point 1 cavern and it measures about 45 m in

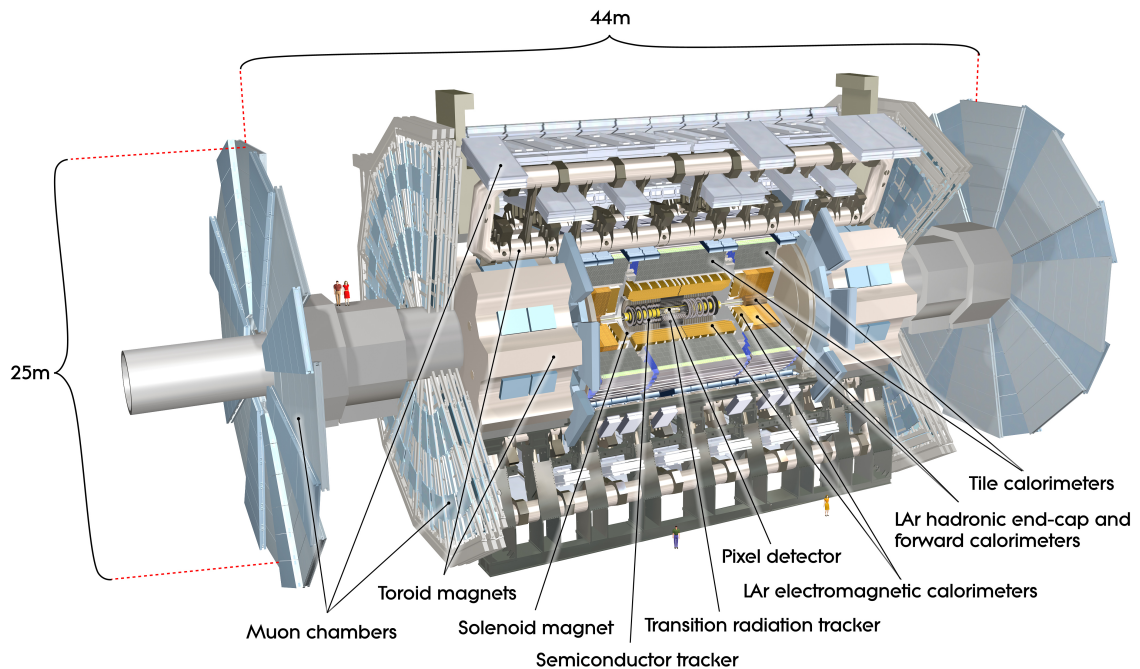


Figure 2.2: Cut-away view of the ATLAS detector. The dimensions of the detector are 25 m in height and 44 m in length. The overall weight of the detector is approximately 7000 tonnes [2].

length and 25 m in diameter. It has a forward-backward symmetric cylindrical geometry with respect to the interaction point and it is designed to reconstruct and measure physics objects such as electrons, muons, photons and hadronic jets. Its design was optimised to be as sensitive as possible to the discovery of the Higgs boson and beyond-the-Standard-Model (BSM) physics. In fact, thanks to the other sub-systems, ATLAS is able to observe all possible decay products by covering nearly 4π steradians of solid angle.

In Figure 2.2 a cut-away view of ATLAS with all its components is shown. The inner-most layer is the Inner Detector (ID) which is the core of the tracking system and consists of a Pixel, a Silicon micro-strip tracker (SCT), and a Transition Radiation Tracker (TRT). It is submerged in a 2 T magnetic field, generated by a thin superconducting solenoid, which bends all the charged particles' trajectories allowing transverse momentum measurement. The electromagnetic and hadronic calorimeters form the next layer and they are both used to perform precise energy measurements of photons, electrons, and hadronic jets. Finally, the outermost layer corresponds to the Muon Spectrometer (MS) which, together with the ID, enclosed in a toroidal magnetic field, allows precise measurement of momentum and position of muons. These sub-detectors will be discussed in more detail in the following sections.

422 **The ATLAS coordinate system**

423 A coordinate system is taken on for the spatial definition of the sub-systems and kin-
424 ematic measurement of physics processes. Such system is defined starting from the in-
425 teraction point, defined as the origin. The z -axis is defined by the beam direction and the
426 $x - y$ plan, as transverse to the beam direction.

427 A quantity, known as pseudorapidity, (η), is defined to describe the angle of a particle
428 coming out of the collision, with respect to the beam axis:

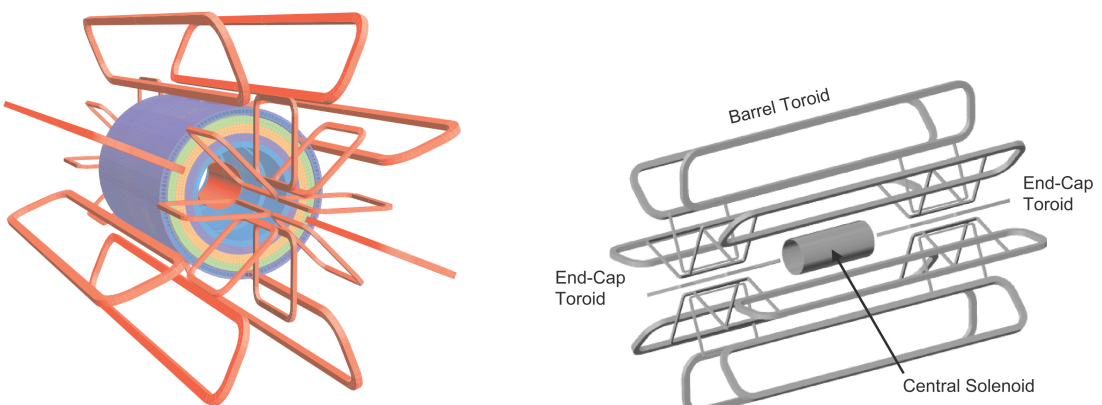
$$\eta \equiv -\ln(\tan(\theta/2))$$

429 Here θ is the polar angle. The azimuthal angle, ϕ , is defined around the beam axis and
430 the polar angle. In the (η, ϕ) space a distance ΔR can be therefore defined as

$$\Delta R = \sqrt{\Delta\eta^2 + \Delta\phi^2}$$

431 where $\Delta\eta$ and $\Delta\phi$ are the differences in pseudorapidity and azimuthal angle between
432 any two considered objects. A central and a forward region of pseudorapidity are also
433 defined such that the detector components are described as part of the *barrel* if they belong
434 to the former or as part of the *end-caps* if they belong to the latter.

435 **2.2.1 The Magnet System**



(a) Geometry of magnet windings and tile calorimeter steel. The eight barrel toroid coils, with the end-cap coils interleaved are visible. The solenoid winding lies inside the calorimeter volume [3].

(b) Schematic view of the superconducting magnets [20].

Figure 2.3: The ATLAS magnet system.

⁴³⁶ The ATLAS magnet system, 26 m long with a 22 m diameter, generates the magnetic
⁴³⁷ field needed to bend the trajectories of charged particles in order to perform momentum
⁴³⁸ measurement. Figure 2.3a and 2.3b show the geometry of the system and its compo-
⁴³⁹ nents, which are made of NbTi - superconducting material - and will be described in the
⁴⁴⁰ following paragraphs.

⁴⁴¹ **The Central Solenoid**

⁴⁴² With an axial length of 5.8 m, an inner radius of 2.46 m, and an outer radius of 2.56 m, the
⁴⁴³ central solenoid magnet is located between the ID and the ECAL. Its function is to bend
⁴⁴⁴ the charged particles that go through the ID and it is aligned on the beam axis providing
⁴⁴⁵ a 2 T axial magnetic field that allows accurate momentum measurement up to 100 GeV
⁴⁴⁶ [20].

⁴⁴⁷ **The Barrel and the End-cap Toroids**

⁴⁴⁸ Figure 2.3b displays the toroid magnetic system that surrounds the calorimeters. With
⁴⁴⁹ its cylindrical shape this component consists of a barrel and two end-caps toroids, each
⁴⁵⁰ with eight superconducting coils. The system allows accurate measurement of muon
⁴⁵¹ momenta using a magnetic field of approximately 0.5 T (barrel) for the central regions
⁴⁵² and 1 T (end-cap) for the end-cap regions, respectively, which bends the particles in the
⁴⁵³ θ direction.

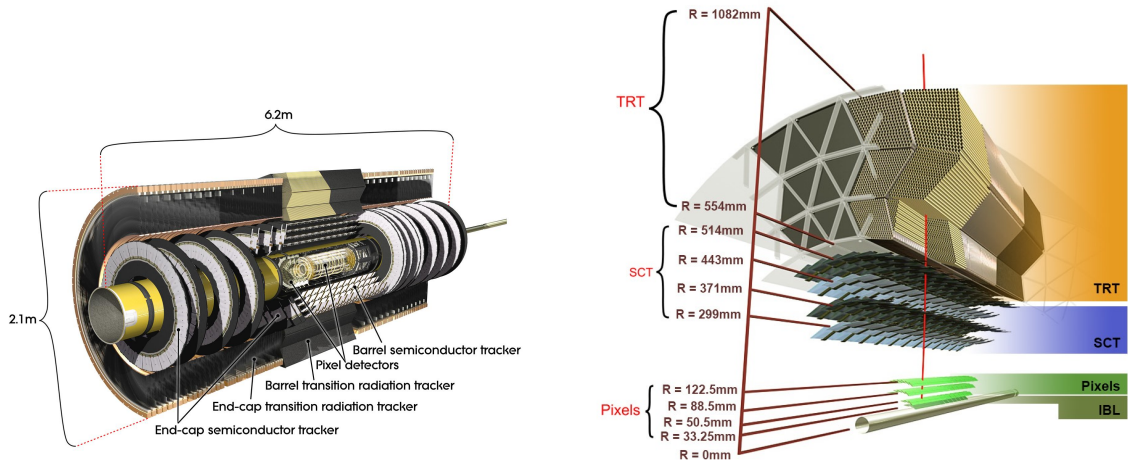
⁴⁵⁴ **2.2.2 The Inner Detector**

⁴⁵⁵ The Inner Detector (ID) [21] is the innermost component of the ATLAS detector i. e. the
⁴⁵⁶ nearest sub-detector to the interaction region and it is used to reconstruct charged particle
⁴⁵⁷ tracks used in the selection of physics objects. In fact, it allows robust track reconstruc-
⁴⁵⁸ tion, with accurate impact parameter resolution ($\sim 20\mu m$) and precise primary and sec-
⁴⁵⁹ ondary vertex reconstruction for charged particles (tracks) above 500 MeV and within
⁴⁶⁰ $|\eta| < 2.5$.

⁴⁶¹ The ID is comprised of independent and concentric sub-systems, which are all shown
⁴⁶² in Figure 2.4:

- ⁴⁶³ • Insertable B-Layer (IBL):

⁴⁶⁴ innermost Pixel Detector layer added during ATLAS Run 2 upgrade (2013/2014) to
⁴⁶⁵ improve vertexing and impact parameter reconstruction;



(a) Overview of the ATLAS ID with labels and dimensions.

(b) Diagram of the ATLAS ID and its sub-detectors.

Figure 2.4: The ATLAS Inner Detector

466 • Silicon Pixel Tracker (Pixel):

467 made of silicon pixel layers and used mainly for reconstructing both the primary
468 and secondary vertices in an event;

469 • SemiConductor Tracker (SCT):

470 comprised of silicon microstrip layers; thanks to its resolution ($17 \times 580 \mu\text{m}$) it can
471 accurately measure particle momenta;

472 • Transition Radiation Tracker (TRT):

473 final layer comprised of various layers of gaseous straw tube elements surrounded
474 by transition radiation material.

475 These sub-detectors will be discussed in the following sections.

476 **IBL**

477 The IBL [22] is the innermost Pixel Detector layer as shown in Figure 2.4b. It is comprised
478 of 6M channels and each pixel measures $50 \times 250 \mu\text{m}$. Its resolution is $8 \times 40 \mu\text{m}$. The
479 addition of this new layer brought a considerable improvement on the performance of the
480 Pixel Detector by enhancing the quality of impact parameter reconstruction of tracks. In
481 particular, this was achieved by improving the vertex finding efficiency and the tagging
482 of bottom-quark-initiated jets (b -jets) which, in case of a B-layer failure, can be restored
483 by the IBL. Besides these improvements, the IBL insertion allowed ATLAS to better cope

⁴⁸⁴ with high luminosity effects such as the increase in event pile-up, which leads to high
⁴⁸⁵ occupancy and read-out inefficiency.

⁴⁸⁶ **Pixel**

⁴⁸⁷ The Pixel detector is comprised of 1750 identical sensorchip-hybrid modules, each cover-
⁴⁸⁸ ing an active area of 16.4×60.8 mm. The total number of modules correspond to roughly
⁴⁸⁹ 80 million semiconductor silicon pixels. The nominal pixel size is $50 \mu\text{m}$ in the ϕ direction
⁴⁹⁰ and $400 \mu\text{m}$ in the barrel region, along the z -axis (beam axis) [23]. The reason why such a
⁴⁹¹ large amount of pixels is employed is justified by the need to cope with the high lumino-
⁴⁹² sity in ATLAS. The silicon pixel detector measures 48.4 cm in diameter and 6.2 m in length
⁴⁹³ providing a pseudorapidity coverage of $|\eta| < 2.5$. Figure 2.4b shows the three concentric
⁴⁹⁴ barrel layers placed at 50.5 mm, 88.5 mm and 122.5 mm respectively. Furthermore, the
⁴⁹⁵ Pixel detector is made of six disk layers, three for each forward region, such that when a
⁴⁹⁶ charged particle crosses the layers it will generate a signal at least in three space points.
⁴⁹⁷ The fine granularity of such detector allows accurate measurement and precise vertex
⁴⁹⁸ reconstruction, as it provides a more accurate position measurement as a large detection
⁴⁹⁹ area is available. In particular, it has a resolution of $10 \times 115 \mu\text{m}$.

⁵⁰⁰ **SCT**

⁵⁰¹ The SCT is made of 4088 modules of silicon micro-strip detectors arranged in four con-
⁵⁰² centric barrel layers. It is mainly used for precise momentum reconstruction over a range
⁵⁰³ $|\eta| < 2.5$ and it was designed for precision measurement of the position using four points
⁵⁰⁴ (corresponding to eight silicon layers), obtained as track hits when crossing the layers.
⁵⁰⁵ Figure 2.4b shows the structure of the SCT with its four concentric barrel layers with
⁵⁰⁶ radii ranging from 299 mm to 514 mm and two end-cap layers. Each module has an in-
⁵⁰⁷ trinsic resolution of $17 \mu\text{m}$ in the $R - \phi$ direction and $580 \mu\text{m}$ in the z direction. As the
⁵⁰⁸ SCT is further away from the beam-pipe than the Pixel detector, it has to cope with re-
⁵⁰⁹ duced particle density. This allows for reduced granularity maintaining the same level of
⁵¹⁰ performance of the Pixel detector: SCT can use ~ 6.3 million read-out channels.

⁵¹¹ **TRT**

⁵¹² The last and outermost of the sub-systems in the ID is the TRT. It is a gaseous detector
⁵¹³ which consists of 4 mm diameter straw tubes wound from a multilayer film reinforced
⁵¹⁴ with carbon fibers and containing a $30 \mu\text{m}$ gold plated tungsten wire in the center. The

straw is filled with a gas mixture of 70% Xe, 27% CO₂ and 3% O₂ [24]. As shown in Figure 2.4b, its section consists of three concentric layers with radii ranging from 544 mm to 1082 mm, each of which has 32 modules containing approximately 50,000 straws, 1.44 m in length, aligned parallel to the beam direction with independent read-out at both ends. Both end-cap sections are divided into 14 wheels, with roughly 320,000 straws in the R-direction. The average 36 hits per track in the central region of the TRT allow continuous tracking to enhance pattern recognition and momentum resolution in the $|\eta| < 2.5$ region. It also improves the p_T resolution for longer tracks.

2.2.3 The Calorimeters

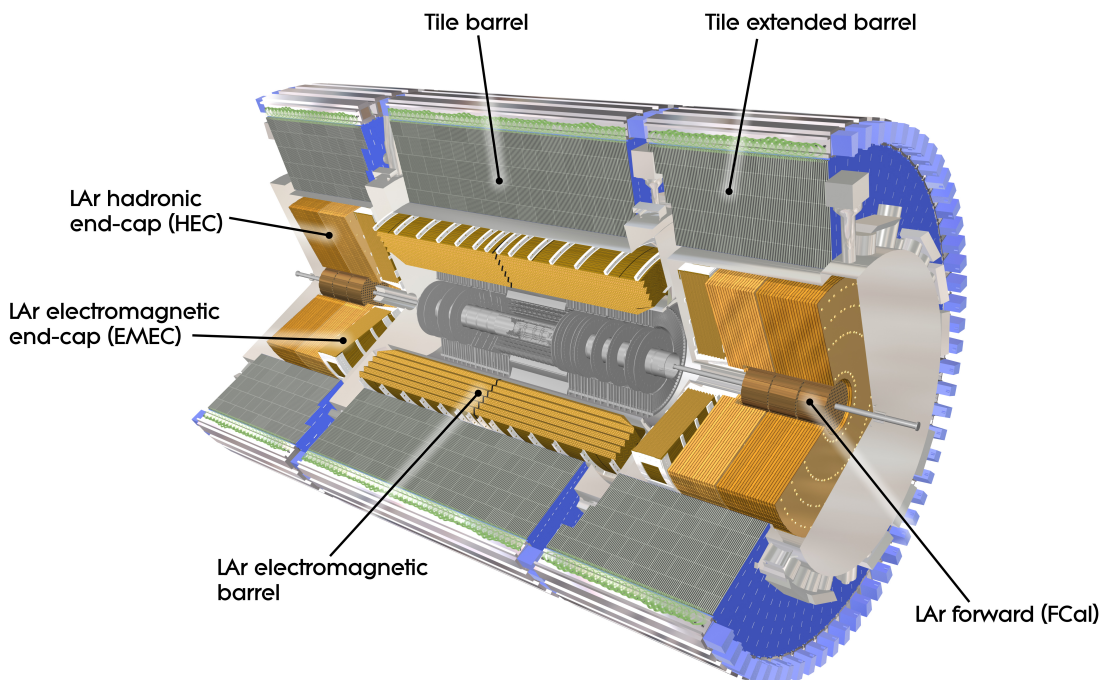


Figure 2.5: A computer generated image of the full calorimeter.

The ATLAS Calorimeter system, shown in Figure 2.5, is comprised of two main subsystems; the electromagnetic calorimeter (ECAL) and hadronic calorimeter (HCAL), which are designed to stop and measure the energy of electromagnetic-interacting and hadronic particles respectively. The combination of the two provides full coverage in ϕ and $|\eta| < 4.95$. Particles slow down and lose energy generating showers when crossing different layers. The ECAL is comprised of one barrel and two end-cap sectors employing liquid Argon (LAr). The showers hereby develop as electrons pairs which are then collected. The HCAL is also comprised of one barrel and two end-cap sectors. The sensors

532 in the barrel of the HCAL are tiles of scintillating plastic whereas LAr is employed for
 533 the end-cap. A forward region, the closest possible to the beam, is covered by a LAr for-
 534 ward calorimeter (FCal). The LAr and Tile Calorimeter will be briefly discussed in the
 535 following paragraphs.

536 **The Liquid Argon Calorimeters**

537 The ECAL is comprised of multiple layers of liquid Argon (LAr) sampler and lead ab-
 538 sorber. The choice of its accordion-geometry design brought two main advantages; full
 539 ϕ coverage with no non-interactive regions (no cracks); fast extraction of signals coming
 540 from both front or rear end of the electrodes. It is made of two half-barrel wheels, both
 541 placed in the barrel cryostat, that provide a pseudorapidity coverage up to $|\eta| < 1.475$
 542 and two end-cap detectors providing $1.375 \leq |\eta| \leq 3.20$ coverage in two end-cap cryo-
 543 stats. The junction between the barrel and end cap components defines the crack region
 544 and any signal coming from the crack region is therefore discarded.

545 In the $|\eta| < 1.8$ region there is an additional layer, placed at the front of the calori-
 546 meter, that is made of a thin (0.5 cm in the end-cap and 1.1 cm in the barrel) LAr layer
 547 with no absorber [25]. This additional layer was designed to correct for the energy lost,
 548 as particles enter the calorimeter, by taking a measurement just before the majority of the
 549 electromagnetic shower is developed.

550 **The Tile calorimeter**

551 The main purpose of the hadronic calorimeter is to measure the energy of hadronic
 552 showers. It is built employing steel and scintillating tiles coupled to optical fibres which
 553 are read out by photo-multipliers. As shown in Figure 2.5, the HCAL is made up of three
 554 cylinders; a central barrel, 5.64 m long covering a region $|\eta| < 1.0$, and two extended
 555 barrel, 2.91 m long covering a reigon $0.8 < |\eta| < 1.7$. Each cylinder is made up of 64
 556 modules and each module is in turn made up of three layers. Ultimately, the smallest
 557 section of the calorimeter module is a cell with a $\Delta\phi \times \Delta\eta = 0.1 \times 0.1$ granularity for the
 558 two innermost layers and $\Delta\phi \times \Delta\eta = 0.2 \times 0.1$ for the outermost one.

559 **2.2.4 The Muon Spectrometer**

560 The MS [26], shown in Figure 2.6, is the outermost sub-system of the whole ATLAS de-
 561 tector. As such, it surrounds the calorimeters and its main function is to perform precision

562 measurement of muons momenta. The deflection of muon tracks employing large super-
 563 conducting air-core toroid magnets and high-precision tracking chambers is at the heart
 564 of such high precision measurement.

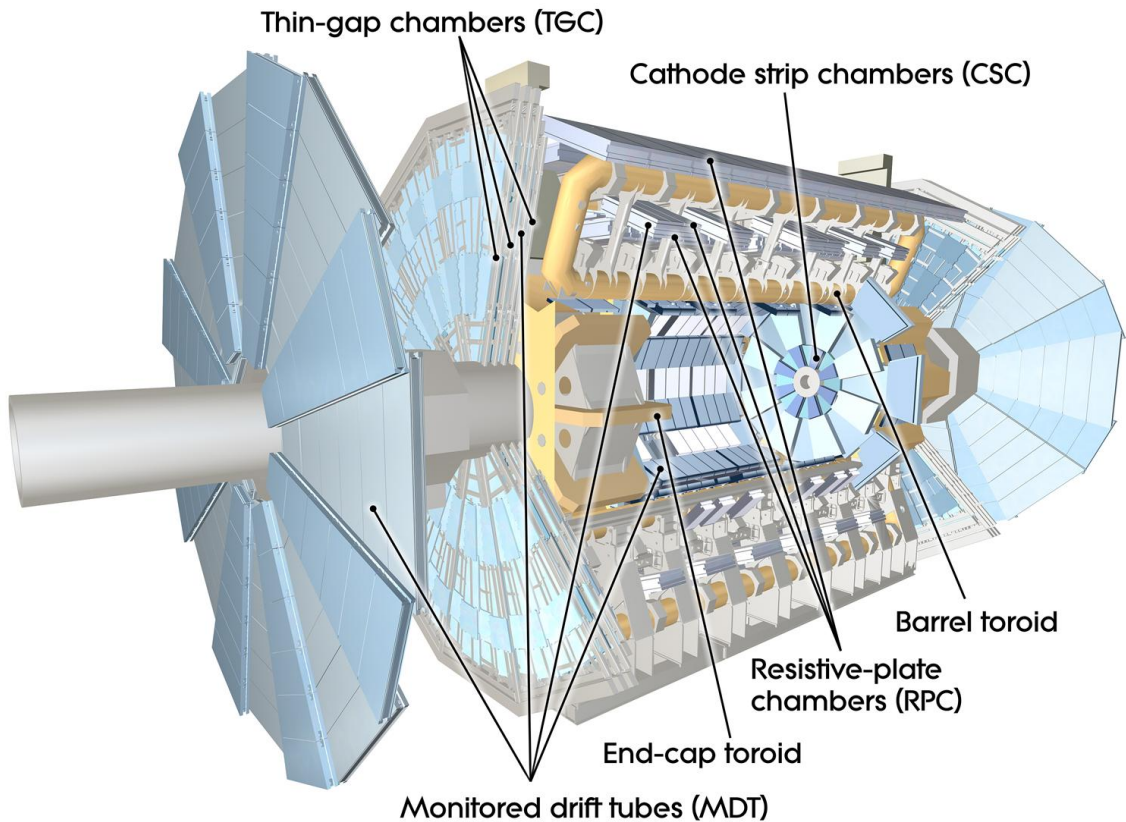


Figure 2.6: Cut-away view of the ATLAS muon system [3].

565 The MS is comprised of one large barrel toroid, covering the region $|\eta| \leq 1.4$, and two
 566 end-cap toroids, covering $1.6 < |\eta| \leq 2.7$ which are employed together to achieve the
 567 track-bending effect wanted. The magnitude of the magnetic field in the barrel, generated
 568 by eight large superconducting coils, ranges from 0.5 to 2 T.

569 Around the beam axis, three cylindrical layers make way for the chambers, placed in
 570 planes perpendicular to the beam, used to measure tracks.

571 Monitored Drift Chambers (MDTs) are employed over most of the pseudorapidity
 572 range to provide precision measurement of track coordinates in the bending direction.
 573 Cathode Strip Chambers (CSCs) are instead employed at large pseudorapidity ($2 < |\eta| <$
 574 2.7). Finally, in the end-cap regions Thin-Gap Chambers (TGCs) together with Resistive-
 575 Plate Chambers (RPCs) are dedicated to the Trigger System discussed in Section 2.3.

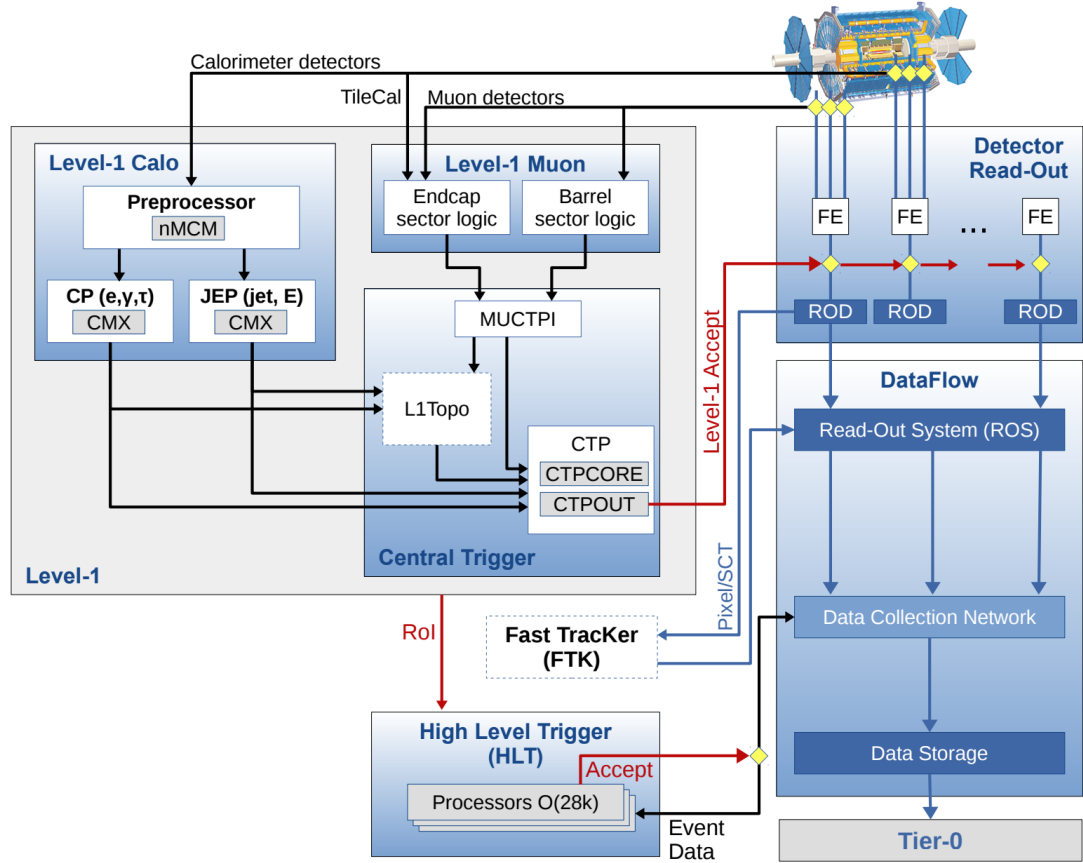


Figure 2.7: The ATLAS TDAQ system. L1Topo and FTK were being commissioned during 2015 and not used for the results shown in this thesis [4].

576 2.3 The ATLAS Trigger System

577 The ATLAS Trigger System is at the heart of data taking. It is an essential component of
 578 any nuclear or particle physics experiment since it is responsible for deciding whether
 579 or not to store an event for later study [4]. The ATLAS Trigger system is employed to
 580 reduce the event rate from ~ 40 MHz¹ bunch-crossing² to ~ 200 Hz which corresponds
 581 to roughly 300 MB/s.

582 The Trigger and Data Acquisition (TDAQ) system shown in Figure 2.7 consists of
 583 a hardware-based first level trigger (L1) and a software-based high-level trigger (HLT).
 584 The L1 trigger decision is formed by the Central Trigger Processor (CTP), which receives
 585 inputs from the L1 calorimeter (L1Calo) and L1 muon (L1Muon) triggers. The first level
 586 (L1), which was designed to perform the first selection step, is a hardware-based system

¹The LHC delivers beams with a bunch-spacing of 25 ns.

²The term bunch-crossing is hereby used when referring to a collision between two bunches of protons.

Since only a certain fraction of the total momentum carried by each proton contributes to the collision, an average number of interactions per bunch-crossing, $\langle \mu \rangle$ is used.

587 that uses information from the calorimeter and muon subdetectors. It also defines the so-
 588 called Regions of Interest (RoIs) within the detector to be investigated by the next level
 589 trigger, the HLT. Additionally, a Fast TracKer (FTK) system [27] (not yet installed) will
 590 provide global ID track reconstruction at the L1 trigger rate using lookup tables stored
 591 in custom associative memory chips for the pattern recognition. The FPGA-based track
 592 fitter will perform a fast linear fit and the tracks are made available to the HLT. This
 593 system will allow the use of tracks at much higher event rates in the HLT than is currently
 594 affordable using CPU systems. However, the upgrade of the ATLAS trigger will not be
 595 discussed any further.

596 In the next sections the L1 and HLT will be briefly described.

597 2.3.1 Level 1 Trigger

598 The Level 1 Trigger identifies Regions of Interest (RoIs)³ and passes these to HLT which
 599 will perform further investigations. Furthermore, in order to decide whether or not the
 600 event processing will continue, L1 selection uses only information coming from some
 601 parts of the detector to keep the input rate to a maximum of 100 kHz. L1 is implemented
 602 in fast custom electronics to keep the latency⁴ below 2.5 μ s. Event data from other sub-
 603 syststem are temporarily stored in memories whilst L1 decision is taken.

604 The L1 topological trigger (L1-Topo) [28] is feeded with energy and direction inform-
 605 ation, about the objects found by the L1 calorimeter and the muon trigger, which will be
 606 processed by dedicated algorithms implemented in its own FPGAs. However, due to the
 607 100 kHz read-out rate, not all the information collected by L1-Topo will be sent to the
 608 HLT, but only part of it. In order to properly seed the ROI-guided HLT reconstruction,
 609 specific objects in combination with the correct topological criteria must be employed.

610 2.3.2 High-Level Trigger

611 The HLT is used to reduce the output rate down to 1 kHz and it has a \sim 200 ms average
 612 decision time. Events that pass L1 trigger are then processed by the HLT using finer-
 613 granularity calorimeter information, precision measurements from the MS and tracking
 614 information from the ID. The HLT reconstruction can be run within RoIs identified at L1
 615 or a so-called full-scan on the full detector can be performed. The track reconstruction in
 616 the Inner Detector is an essential component of the trigger decision in the HLT and it will

³ $\eta - \phi$ regions where event features have been found by the L1 selection process.

⁴Time needed by an electric signal to get to the front-end electronics.

- ⁶¹⁷ be discussed more in detail in Chapter 3

618 Chapter 3

619 The *b*-jet Trigger Signature in ATLAS

620 In this chapter the monitor and performance of the bottom-quark-initiated jet (*b*-jet) sig-
621 nature trigger, this being the author’s “technical/qualification task” to become a qualified
622 member of the experiment, will be discussed. The efficiencies of some of the Run 2 *b*-jet
623 triggers were evaluated using 3.8 fb^{-1} of pp collisions data collected in 2015 with 25 ns
624 bunch-spacing.

625 The qualification task

626 3.1 Trigger Efficiency

627 **Chapter 4**

628 **Event Simulation and Reconstruction**

629 bla bla bla

630 **4.1 Event Generation**

631 bla bla

632 **4.1.1 Parton Distribution Functions (PDFs)**

633 bla bla bla

634 **4.1.2 Matrix Element Calculation**

635 bla bla bla

636 **4.1.3 Parton Showers**

637 bla bla bla

638 **4.1.4 Hadronisation**

639 bla bla bla

640 **4.2 Detector Simulation**

641 bla bla bla

642 **Chapter 5**

643 **Stop searches in final states with jets
and missing transverse energy**

⁶⁴⁵ **Chapter 6**

⁶⁴⁶ **Results and Statistical Interpretations**

647 Trigger

648 bla vlas bla

Bibliography

- [1] ATLAS Collaboration, "Summary plots from the atlas standard model physics group."
https://atlas.web.cern.ch/Atlas/GROUPS/PHYSICS/CombinedSummaryPlots/SM/ATLAS_a_SMSummary_TotalXsect/ATLAS_a_SMSummary_TotalXsect.png. viii, 9
- [2] C. Lefèvre, *The CERN accelerator complex.*, <http://cds.cern.ch/record/1260465>. viii, 14, 15
- [3] ATLAS Collaboration, *The ATLAS experiment at the CERN Large Hadron Collider*, Journal of Instrumentation **3** no. 08, (2008) S08003.
<http://stacks.iop.org/1748-0221/3/i=08/a=S08003>. viii, 16, 22
- [4] A. Collaboration, *Performance of the ATLAS Trigger System in 2015*, Eur. Phys. J. **C77** (2017), [arXiv:1611.09661 \[hep-ex\]](https://arxiv.org/abs/1611.09661). viii, 23
- [5] M. Herrero, *The Standard Model.*, <https://arxiv.org/abs/hep-ph/9812242>. 3
- [6] ATLAS Collaboration, *Observation of a New Particle in the Search for the Standard Model Higgs Boson with the ATLAS Detector at the LHC*, Phys.Lett. **B716** (2012), [arXiv:1207.7214 \[hep-ex\]](https://arxiv.org/abs/1207.7214). 3
- [7] CMS Collaboration, *Observation of a new boson at a mass of 125 GeV with the CMS experiment at the LHC*, Phys.Lett. **B716** (2012), [arXiv:1207.7235 \[hep-ex\]](https://arxiv.org/abs/1207.7235). 3
- [8] A. Pich, *The Standard Model of Electroweak Interactions*, [arXiv:1201.0537 \[hep-ph\]](https://arxiv.org/abs/1201.0537). 5, 7
- [9] K. A. Olive at al. (Particle Data Group), *Review of Particle Physics*, Chin.Phys. C **38(9)** (2014). 6
- [10] J. Goldstone, A. Salam and S. Weinberg, *Broken Symmetries*, Phys. Rev. **127** (1962) 965–970. 8

- 673 [11] S. Weinberg, *Implications of Dynamical Symmetry Breaking*, Phys. Rev. **D19** (1976)
 674 1277–1280. 10
- 675 [12] Super-Kamiokande Collaboration, Y. Fukuda et al., *Evidence for oscillation of*
 676 *atmospheric neutrinos*, Phys. Rev. Lett. **81** (1998) 1562–1567, arXiv:hep-ex/9807003
 677 [hep-ex]. 10
- 678 [13] SNO Collaboration, *Measurement of the Rate of $\nu_e + d \rightarrow p + p + e^-$ Interactions*
 679 *Produced by 8B Solar Neutrinos at the Sudbury Neutrino Observatory*, Phys. Rev. Lett.
 680 **87** (2001). 10
- 681 [14] T. O. W. of the Nobel Prize.
 682 https://www.nobelprize.org/nobel_prizes/physics/laureates/2015/. 10
- 683 [15] J.M. Jowett, M. Schaumann, R. Alemany, R. Bruce, M. Giovannozzi, P. Hermes, W.
 684 Hofle, M. Lamont, T. Mertens, S. Redaelli, J. Uythoven, J. Wenninger, *The 2015*
 685 *Heavy-Ion Run of the LHC*,
 686 <http://accelconf.web.cern.ch/accelconf/ipac2016/papers/tupmw027.pdf>. 13
- 687 [16] O. S. Brüuning, P. Collier, P. Lebrun, S. Myers, R. Ostojic, J. Poole and P. Proudlock,
 688 *LHC Design Report*, <https://cds.cern.ch/record/782076>. 14
- 689 [17] CMS Collaboration, *The CMS experiment at the CERN LHC*, Journal of
 690 Instrumentation **3** no. 08, (2008) S08004.
 691 <http://stacks.iop.org/1748-0221/3/i=08/a=S08004>. 14
- 692 [18] LHCb Collaboration, et. al, *The LHCb Detector at the LHC*, JINST (2008). 14
- 693 [19] ALICE Collaboration, *The ALICE experiment at the CERN LHC*, Journal of
 694 Instrumentation **3** no. 08, (2008) S08002.
 695 <http://stacks.iop.org/1748-0221/3/i=08/a=S08002>. 14
- 696 [20] A. Yamamoto, Y. Makida, R. Ruber, Y. Doi, T. Haruyama, F. Haug, H. ten Kate,
 697 M. Kawai, T. Kondo, Y. Kondo, J. Metselaar, S. Mizumaki, G. Olesen, O. Pavlov,
 698 S. Ravat, E. Sbrissa, K. Tanaka, T. Taylor, and H. Yamaoka, *The ATLAS central*
 699 *solenoid*, Nuclear Instruments and Methods in Physics Research Section A:
 700 Accelerators, Spectrometers, Detectors and Associated Equipment **584** no. 1, (2008)
 701 53 – 74.
 702 <http://www.sciencedirect.com/science/article/pii/S0168900207020414>. 16,
 703 17

- 704 [21] ATLAS Collaboration, *The ATLAS Inner Detector commissioning and calibration*, *Eur.*
705 *Phys. JC***70**, [arXiv:1004.5293](https://arxiv.org/abs/1004.5293). 17
- 706 [22] ATLAS Collaboration, *ATLAS Insertable B-Layer Technical Design Report*,
707 <https://cds.cern.ch/record/1291633>. 18
- 708 [23] G. A. et al., *ATLAS pixel detector electronics and sensors*, *Journal of Instrumentation* **3**
709 no. 07, (2008) P07007. <http://stacks.iop.org/1748-0221/3/i=07/a=P07007>. 19
- 710 [24] A. Bingül, *The ATLAS TRT and its Performance at LHC*, *Journal of Physics:*
711 *Conference Series* **347** no. 1, (2012) 012025.
712 <http://iopscience.iop.org/article/10.1088/1742-6596/347/1/012025/meta>.
713 20
- 714 [25] ATLAS Collaboration, *ATLAS liquid-argon calorimeter: Technical Design Report*,
715 <https://cds.cern.ch/record/331061>. 21
- 716 [26] ATLAS Collaboration, *ATLAS muon spectrometer: Technical design report*,
717 <https://cds.cern.ch/record/331068>. 21
- 718 [27] ATLAS Collaboration, *Fast TrackEr (FTK) Technical Design Report*,
719 <https://cds.cern.ch/record/1552953>. 24
- 720 [28] E. Simoni, *The Topological Processor for the future ATLAS Level-1 Trigger: from design to*
721 *commissioning*, [arXiv:1406.4316](https://arxiv.org/abs/1406.4316). 24